A Biomimetic, 4.5μW, 120+dB, Log-domain Cochlea Channel with AGC

A. G. Katsiamis, *Student, Member IEEE*, E. M. Drakakis, *Member, IEEE* and R. F. Lyon, *Fellow, IEEE*

***Abstract*—This paper deals with the design and performance evaluation of a new analogue CMOS cochlea channel of increased biorealism. The design implements a recently proposed transfer function, namely the One-Zero Gammatone Filter (or OZGF), which provides a robust foundation for modeling a variety of auditory data such as realistic passband asymmetry, linear low-frequency tail and level-dependent gain. Moreover, the OZGF is attractive because it can be implemented efficiently in any technological medium – analogue or digital – using standard building blocks. The channel was synthesized using novel, low-power, Class-AB, log-domain, biquadratic filters employing MOS transistors operating in their weak inversion regime. Furthermore, the paper details the design of a new low-power automatic gain control circuit that adapts the gain of the channel according to the input signal strength, thereby extending significantly its input dynamic range. We evaluate the performance of a 4th-order OZGF channel (equivalent to an 8th-order cascaded filter structure) through both detailed simulations and measurements from a fabricated chip using the commercially available 0.35μm AMS CMOS process. The whole system is tuned at 3kHz, dissipates a mere 4.46μW of static power, accommodates 124dB (at <5% THD) of input dynamic range at the center frequency and is set to provide up to 70dB of amplification for small signals.**

***Index Terms*—auditory processing, bionic ear, cochlea, companding, gammatone, log-domain, low-power**

I. Introduction

THE recent upsurge in research activity in the field of neuromorphic engineering – a term coined in the early 80s by Carver Mead [1] – has led to the successful development of artificial/engineered systems, which either mimic or partly draw inspiration from a plethora of operations observed from biological systems encountered in nature. These research efforts are motivated both by the need to understand the underlying engineering strategies that nature had to develop during the evolution of intelligent animal behavior and the growing demand for miniaturized, power-efficient solutions.

This paper tries to advance the neuromorphic engineering field by using inherently compressive frequency shaping networks to realize a recently proposed auditory filter of promising frequency-domain attributes. In particular, this paper addresses the CMOS implementation of a new practical analogue cochlea channel (suitable for filterbank-type applications) together with its automatic gain control (AGC) mechanism. The design is implemented using micropower companding techniques. Emphasis is given to the evaluation of the technical performance characteristics of the whole channel.

The paper is organized as follows: In Section II we briefly outline previous important work on low-power CMOS analogue cochlea design. In Section III we briefly present the transfer function of the One-Zero Gammatone Filter together with a summary of its unique characteristics that render it an ideal candidate for efficient cochlea processing especially in the analogue domain. Section IV describes the basic motivation for using log-domain as our main circuit design vehicle in achieving high dynamic range (DR) and low-power performance. In Section V we describe in detail all the circuits, whereas in section VI we disseminate detailed measured results from a fabricated chip in the 0.35μm AMS CMOS process. In section VII we summarize our findings and conclude.

II. The CMOS Cochlea

One of the first biological systems to be studied meticulously by the VLSI community was the inner ear or cochlea (other examples that followed are the retina, the neuron and the pancreatic beta-cells to mention just a few). For more than twenty-five years, engineers have tried extensively to replicate in silicon certain anatomical and/or operational characteristics of the cochlea in order to create an artificial system that shares, to a great extent, the outstanding properties of its biological counterpart.

The first attempt was from R. F. Lyon who proposed in 1982 a computational model of filtering, detection and compression in the cochlea [2]. In that work, the 3-dimensional electro-hydro-mechanical properties of the basilar membrane (the basic structure that performs frequency decomposition and filtering) were modeled as an 1-dimensional cascade of linear time-invariant resonant 2nd-order transfer functions or sections, whose pole frequencies did not coincide but varied in a predefined geometrically decreasing fashion. Lyon also proposed a distributed nonlinear AGC scheme that provided straight gain variation at each of the output taps of the cascade with the gain control responding to the system's output level. Six years later, his 1988 effort co-authored with Carver Mead [3-5], was the first attempt to link the so-called

Manuscript received October 9, 2001. This work was supported by the Engineering and Physical Sciences Research Council (EPSRC) UK under Grant GR/S69269/01.

A. G. Katsiamis is with the Department of Bioengineering (The Sir Leon Bagrit Centre), Imperial College London, South Kensington Campus SW7 2AZ UK (phone: +44 (0)20 7594 5664; fax: +44 (0)20 7584 6897; e-mail: katsiamis@ imperial.ac.uk).

E. M. Drakakis is with the Department of Bioengineering (The Sir Leon Bagrit Centre), Imperial College London, South Kensington Campus SW7 2AZ UK (phone: +44 (0)20 7594 5182; fax: +44 (0)20 7584 6897; e-mail: e.drakakis@ imperial.ac.uk).

R. F. Lyon is with Google, Inc., 1600 Amphitheatre Parkway Mountain View, CA 94043 (e-mail: dicklyon@acm.org).

'Lyon Cochlear Model' with VLSI-compatible structures and to demonstrate a fully operational electronic system that hears. Contrary to what he had proposed in [2], here transduction and nonlinear compression (attributed to the operation of the inner- and outer-hair cells, IHC and OHC, respectively) were modeled communally as a local, fast-acting, gain control mechanism that adapted the values of the quality factors (Q) for each of the individual sections of the cascade according to input signal strength. However, no experimental results employing AGC circuits were presented, most probably due to several stability issues they were facing at the time [6]. The open-loop case was demonstrated but no detailed performance figures like noise, distortion etc., were reported. In the years that followed, the open-loop CMOS cochlea saw several improved embodiments in the hands of Lloyd Watts [7] and Andre Van Schaik [8], but the emphasis remained on the overall synthesis side rather than on the performance evaluation side. Subsequently, Sarpeshkar was the first to demonstrate and more importantly evaluate an electronic cochlea with an active AGC scheme [9;10]. His design employed several circuit techniques to widen the linear range of the operational transconductance amplifiers (OTA) involved, confine the noise propagation and cancel the offset accumulation between filter stages. All these techniques were published extensively and can be found collectively in [11]. To our opinion, Sarpeshkar's cochlea design remains to this date one of the most well-crafted engineering efforts. Many other notable implementations can be found in the literature (e.g. [12-21]), including some that also utilize the same current-mode techniques to the ones described in this work, but are either lacking the accuracy in terms of biological fidelity (frequency response and/or AGC) or the detailed performance evaluation.

III. The One-Zero Gammatone Filter

As outlined previously, the design of the cochlea channel described in this work is based on the analogue circuit implementation of a particular novel auditory filter called the One-Zero Gammatone Filter, termed thereafter OZGF. The OZGF is a variant of the well-known Gammatone Filter (GTF) proposed by Johannesma in 1972 [22] and was introduced by Lyon in 1996 [23] as an efficient auditory filter in terms of both its relative ease of hardware implementation and its simple mathematical parameterization.

The GTF, from which the OZGF is derived, is one of the most commonly used transfer functions in the auditory modeling community and is described in the Laplace-domain by (1); ω_o is the natural or pole frequency, N is the gammatone order, Q is the quality factor and ϕ is the phase. Yet, the 'spurious' zeros appearing in the numerator of (1) are a limitation if one considers the GTF as a potential candidate for analogue hardware realizations. Apart from the fact that it is seems rather complicated to design such a filter using standard analogue filtering design techniques (note that all implementations of the GTF reported to date are digital), the interaction between the two N^{th}-order complex zero terms, which add with constructive or destructive interference according to the particular values of N, Q and ϕ, render its behavior unrealistic when trying to incorporate level-dependent changes in the response (i.e. gain control). Moreover, Patterson and Nimmo-Smith observed that the GTF is nearly symmetric in the passband, while physiological evidence shows a significant asymmetry in the biological cochlea transfer function [24]. Irino was the first to address the GTF-symmetry issue by proposing a new asymmetric auditory filter of the gammatone family called the Gammachirp [25]. The Gammachirp is essentially a cascade of a passive GTF with an asymmetric function with varying center frequency to introduce level-dependence. The Gammachirp has been successful in fitting to various physiological data [26;27], but seems even more daunting implementation-wise than the simple GTF, since it cannot be expressed as a rational transfer function.

$$H_{GTF}(s)=\frac{\left\{\begin{array}{l} e^{j\phi}\left[s+\frac{\omega_o}{2Q}+j\omega_o\sqrt{1-\frac{1}{4Q^2}}\right]^N+ \\ +e^{-j\phi}\left[s+\frac{\omega_o}{2Q}-j\omega_o\sqrt{1-\frac{1}{4Q^2}}\right]^N \end{array}\right\}}{[s^2+\frac{\omega_o}{Q}s+{\omega_o}^2]^N} \qquad (1)$$

The OZGF transfer function, described in (2), is derived from the GTF by discarding all but one of its zeros, with that zero lying anywhere on the real axis. From the implementation point of view, an N^{th}-order OZGF can be considered as the composition of two individual transfer functions; a cascade of (N–1) identical lowpass (LP) biquadratic filters – otherwise known as an $(N-1)^{\text{th}}$-order All-Pole Gammatone Filter (or APGF) [23;28] – coupled with an appropriately scaled lossy bandpass (BP) biquadratic filter i.e. a 2-pole, 1-zero resonant transfer function:

$$H_{OZGF}(s)=\frac{{\omega_o}^{2N-1}(s+\omega_z)}{[s^2+\frac{\omega_o}{Q}s+{\omega_o}^2]^N}$$

$$=\underbrace{\frac{{\omega_o}^{2N-2}}{[s^2+\frac{\omega_o}{Q}s+{\omega_o}^2]^{N-1}}}_{\substack{(N-1)\text{ cascaded LP biquads} \\ \text{or } (N-1)^{\text{th}}\text{-order APGF}}}\times\underbrace{\frac{\omega_o(s+\omega_z)}{s^2+\frac{\omega_o}{Q}s+{\omega_o}^2}}_{\substack{\text{lossy BP biquad} \\ \text{or 2-pole, 1-zero transfer function}}} \qquad (2)$$

The OZGF, albeit relatively unknown, is a very important filter for the auditory modeling/engineering community because it exhibits the following unique characteristics:

- It provides an appropriately shaped 'pseudo-resonant' frequency-domain response that can be used to reasonably match psychoacoustic data.
- It has a realistic asymmetry in the passband.
- It has a simple parameterization; the gain, bandwidth and passband asymmetry are all correctly coupled via the variation of a single controllable parameter in its transfer function: its quality factor Q.
- It maintains a linear tail for frequencies well below the center frequency as the Q is varied.
- It can efficiently be implemented in hardware or software and in any technology; it is a simple cascade of biquadratic filters with identical pole locations.
- It provides a logical link to Lyon's neuromorphic (traveling-wave) cascade model of the underlying cochlea mechanics.

- It does not suffer from the excessive delay naturally occurring in cochlea designs employing long-cascade of all-pole transfer functions.

Fig. 1 depicts the frequency response obtained from the mammalian cochlea, whereas Fig. 2 the frequency response of a 4th-order OZGF with varying *Q*. For a thorough treatment regarding the parameterization and characterization of the OZGF transfer function the reader is referred to [29].

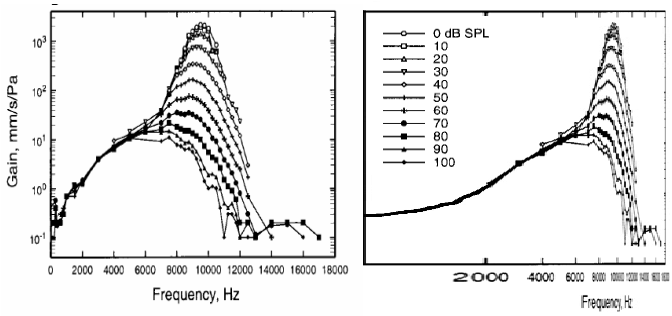

Fig. 1: The biological cochlea transfer function for various levels of input strength (measured in dB of sound pressure level – dB SPL) adapted from Ruggero et al [30].The original graph (left) was treated using the interp2 function in MatLab™ to convert the frequency axis into log-scale and aid direct comparison with Fig. 2. Observe that for a linear dB SPL change in input intensity the peak of the cochlea characteristic changes linearly.

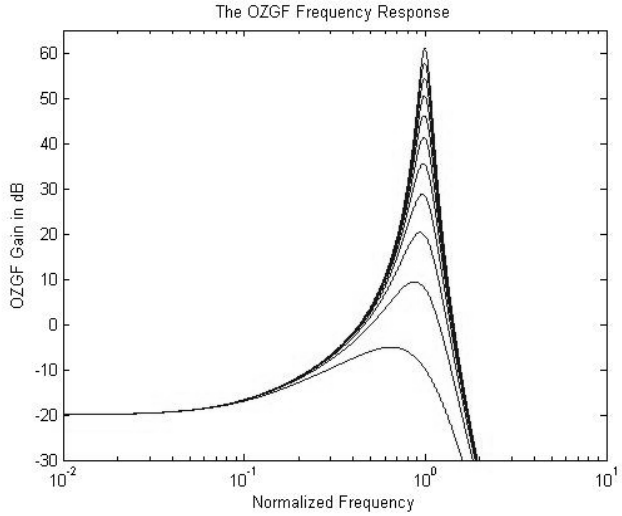

Fig. 2: The OZGF frequency response of order 4 and with *Q* varying from 0.75 to 6. The zero was placed at a frequency 1/10 of the natural frequency resulting in a –20dB gain at DC like in the physiological data of Fig. 1. The frequency axis is normalized to the natural frequency.

IV. Architectural Design Considerations

The first generations of high performance cochlea designs were synthesized using g_m-C filters and relied on power-hungry linearization techniques and/or the compressive action of the AGC for extending the input DR. However, recent advances in the field of analogue filter design have led to the development of inherently compressive systems that operate internally in the nonlinear domain while preserving overall input-output linearity.

The application of companding in filter design resulted in the successful realization of topologies that were able to attain a wider input DR with a lower power supply requirement compared to traditional g_m-C filters employing linearized transconductors. These companding filters or processors belong to the more general class of ELIN (Externally-Linear–Internally-Nonlinear) systems [31] and their systematic synthesis is articulated in the pioneering works of Frey [32] and Tsividis [33]. It is worth noting that the need for inherently compressive filters emerged very early in the development process of micropower, high DR cochlea designs and in fact a bit earlier than the first 1993 log-domain paper by Frey [34] – check pp.1 under the section 'Cochlea Improvements' of [6].

Since Frey's 1993 paper, log-domain circuits progressed significantly with several contributions aiming at increasing the input DR and lowering the quiescent power dissipation. The two most thoroughly studied techniques are: a) the use of two Class-A filters in a pseudo-differential Class-AB arrangement [35;36] that increases the DR without spending too much power and b) the use of an AGC scheme that dynamically changes certain biasing levels of the filter (according to a particular measure of input signal strength) in order to optimize its output SNR and power dissipation – this technique is otherwise known as syllabic companding [37;38] and constitutes a parallel engineering strategy to the one performed by the real cochlea to widen its input DR and maintain signal integrity. It is interesting to note that several mechanisms within the cochlea may include an adjustable 'DC bias' in the basilar membrane caused by hair cell interactions that affect the operating point on their detection nonlinearity and their sensitivity [2].

In the following sections, we discuss the proposed pseudo-differential, Class-AB, log-domain implementation of a 4th-order (i.e. a cascade of four, 2nd-order transfer functions) OZGF with the ability to automatically adapt its gain by means of a low-power, current-mode AGC circuit acting in feed-forward. The AGC senses the strength of the input signal and according to a particular control law sets the *Q* values of the individual filter stages of the cascade comprising the channel. The action of the AGC helps accommodate a wider input DR: when the input is small (say below or close to the noise floor), the OZGF adapts its gain and provides significant amplification for the output to be well above noise levels. On the other hand, when the input is large, the OZGF provides low or no amplification so that acceptable distortion levels at the output are maintained. Since, in effect, the AGC is changing the state-variables or pole-positions of the individual filters, the whole OZGF channel falls under the category of a *high-order, syllabically companding, ELIN, auditory amplifier/processor.*

Fig. 3 depicts the high-level block diagram of our active 4th-order OZGF channel architecture. It should be noted here that by the term 'active' we refer to the channel together with its feed-forward AGC mechanism to discriminate from its 'without-AGC open-loop' case where all the biasing currents controlling its gain are set manually; from now on we will refer to this case as simply 'open-loop'. In addition, we chose to employ a feed-forward scheme (like the one demonstrated in [10]) as opposed to a feedback (like in [39]) in order to avoid any latency issues and obtain faster adaptation times.

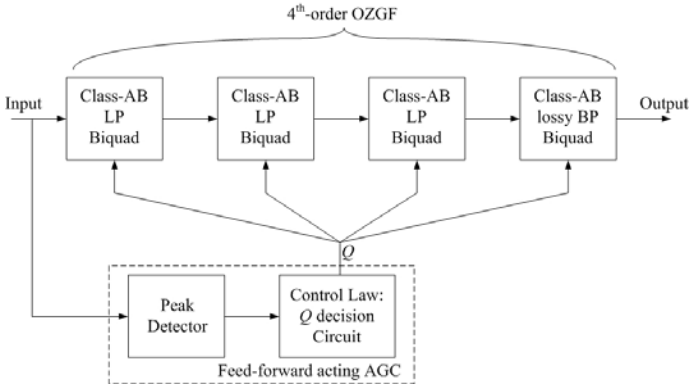

Fig. 3: Block diagram of the active 4th-order OZGF channel.

V. The Circuits

This section deals with the design of the circuits comprising the 4th-order OZGF channel with its AGC. All device sizes, biasing currents, capacitors and power supplies are displayed on TABLE I in section V.D.

A. Pseudo-differential Class-AB Log-domain Biquads

Class-AB designs are offered as the most efficient solution for balancing DR and low quiescent power consumption performance requirements. This is because for small-signals a Class-AB design operates with the quality of a Class-A system, whereas for large-signals with the efficiency of a Class-B system.

In log-domain, one way to design a Class-AB filter is by connecting two Class-A filters in a pseudo-differential arrangement with a signal conditioner at the input. The signal conditioner ensures that a bi-directional input signal is split into two complementary, uni-directional, positive signals, which are then processed separately by the two Class-A filters. The respective uni-directional processed outputs are subsequently subtracted to form the total bi-directional output, which is a linearly filtered version of the input (see Fig. 4). However, this is not enough to guarantee Class-AB operation unless the following two rules (implied by the vertical, two-sided arrows depicted in Fig. 4) are obeyed [36]:

a. Firstly, a non-zero dc-operating point solution must always exist for all the state-variables (these are currents in log-domain filter implementations) for any strictly positive, static (i.e. dc) values of the complementary inputs. This can be achieved by ensuring that the derivatives of the state-variables can become equal to zero while the state-variables themselves remain strictly positive.

b. Secondly, all state-variables must remain strictly positive provided that the complementary inputs remain strictly positive and bounded for all time. This can be achieved by enforcing the derivative of a state-variable to be strictly positive in the limit as the variable approaches zero; hence, that variable can never reach zero and thus will stay strictly positive for all time.

In short, the above two rules state that in a transistor-level implementation of a Class-AB log-domain topology, all devices should carry non-zero and strictly positive currents at all times.

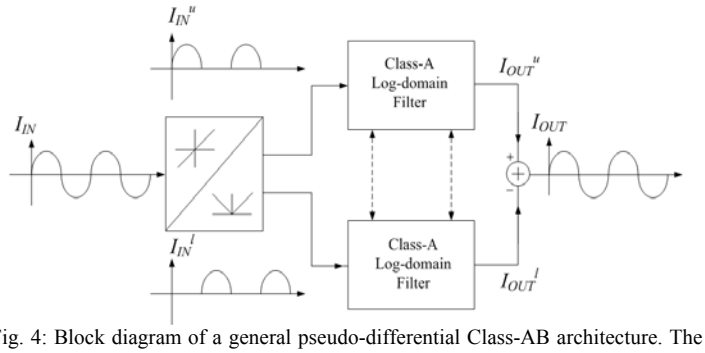

Fig. 4: Block diagram of a general pseudo-differential Class-AB architecture. The two vertical arrows between the two Class-A filters indicate coupling that ensures correct Class-AB operation.

One possible Class-AB-compatible state-space description for a differential biquad is given below [36]:

$$
\begin{aligned}
u &= u_u - u_l \\
\dot{x}_{u1} &= \omega_o\left(-\frac{1}{Q}x_{u1} + x_{l2} + u_u - \frac{x_{u1}x_{l1}}{g}\right) \\
\dot{x}_{u2} &= \omega_o\left(x_{u1} - \frac{x_{u2}x_{l2}}{g}\right) \\
\dot{x}_{l1} &= \omega_o\left(-\frac{1}{Q}x_{l1} + x_{u2} + u_l - \frac{x_{u1}x_{l1}}{g}\right) \\
\dot{x}_{l2} &= \omega_o\left(x_{l1} - \frac{x_{u2}x_{l2}}{g}\right) \\
y_{BP} &= x_{u1} - x_{l1}\,;\, y_{LP} = x_{u2} - x_{l2}
\end{aligned}
\tag{3}
$$

where u is the differential input, y_{LP}, y_{BP} are the LP and BP differential outputs, respectively and g is a positive factor that depends on implementation and will be defined later on. The subscripts u and l denote 'upper' and 'lower' referring to the two individual Class-A filter branches. The interested reader could verify that the derivatives $\dot{x}_{uj}$, $\dot{x}_{lj}$ (j=1, 2) always attain a positive value whenever their respective state-variables tend to zero, or in other words to guarantee the existence of a DC operating point (condition a). Also, nonlinear cross-coupling terms of the form $x_{uj}x_{lj}$ (j=1, 2) have been added to ensure that the derivatives can reach a zero value while the state-variables themselves remain strictly positive. Since the outputs are formed differentially, the nonlinear cross-coupling terms cancel out ensuring an overall linear characteristic. The next section describes the transistor-level log-domain implementation of (3) using the Bernoulli Cell (BC) Formalism.

Biquad Synthesis via the Bernoulli Cell Formalism

The BC was introduced in [40]as a low-level operator for synthesizing log-domain filters. It consists of an exponential transconductor and a grounded capacitor and through a nonlinear change of its state-variable linearizes and electronically solves a nonlinear differential equation of the well-known Bernoulli form (see Fig. 5). A cascade of BC is known as the 'Bernoulli backbone' and implements a generic set of differential equations termed Log-Domain State-Space or LDSS. Such a 'backbone' is depicted in the log-domain biquad implementation of Fig. 7 which realizes the state-space equations shown in (3). In Fig. 7, the BCs are denoted by circles, each consisting of a PMOS-WI transistor and a capacitor connected between its source terminal and ground.

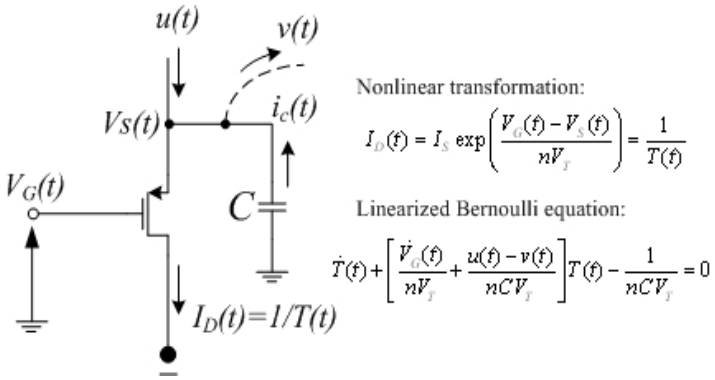

Fig. 5: Logarithmically driven Bernoulli Cell together with the nonlinear transformation and linearized differential equation that it solves.

The transistor-level synthesis procedure is based on the direct comparison of the required dynamics of the original prototype system (i.e. (3)) with those codified by the LDSS equations; the scope of this comparison is to identify the necessary time-domain relations (implemented by means of static translinear loops) that modify the LDSS dynamics in such a way so that they become identical to the desired ones [41].

Having in mind a MOS-WI implementation, the two generic LDSS equations describing a Class-A 2nd-order system (i.e. the differential equations describing two interconnected, logarithmically driven BCs [40;41]) are:

$$\begin{aligned} nCV_T\dot{w}_1 + (u_1 - v_1)w_1 &= I_{IN} \\ nCV_T\dot{w}_2 + (u_2 - v_2)w_2 &= w_1 \end{aligned} \tag{4}$$

with the *w*-variables being defined as:

$$\begin{aligned} w_1 &\propto T_1 I_{IN} \\ w_2 &\propto T_2 T_1 I_{IN} = T_2 w_1 \end{aligned} \tag{5}$$

By appropriately defining the *u*, *v* currents via translinear loops (as can be verified by examining the topology in Fig. 7 together with (7)), the LDSS equations are modified and described in differential form as:

$$\begin{aligned} nCV_T\dot{w}_{u1} + (I_Q + I_o w_{l1})w_{u1} &= {I_{IN}}^u + {I_o}^2 w_{l2} \\ nCV_T\dot{w}_{u2} + ({I_o}^2 w_{l2})w_{u2} &= w_{u1} \\ nCV_T\dot{w}_{l1} + (I_Q + I_o w_{u1})w_{l1} &= {I_{IN}}^l + {I_o}^2 w_{u2} \\ nCV_T\dot{w}_{l2} + ({I_o}^2 w_{u2})w_{l2} &= w_{l1} \end{aligned} \tag{6}$$

with the *w* state-variables being now defined as:

$$\begin{aligned} w_{u1} &= I_o\left[T_{u1}\left({I_{IN}}^u + w_{l2}\right)\right] \\ w_{u2} &= {I_o}^2\left[T_{u2}T_{u1}\left({I_{IN}}^u + w_{l2}\right)\right] = I_o T_{u2} w_{u1} \\ w_{l1} &= I_o\left[T_{l1}\left({I_{IN}}^l + w_{u2}\right)\right] \\ w_{l2} &= {I_o}^2\left[T_{l2}T_{l1}\left({I_{IN}}^l + w_{u2}\right)\right] = I_o T_{l2} w_{l1} \end{aligned} \tag{7}$$

In (4)–(7), the parameters *C, n* and V_T denote the grounded capacitors, the subthreshold slope parameter (typically between 1 and 2) and the thermal voltage (25mV@T=300K), respectively. In addition, ${I_{IN}}^{u,l}$ are the two upper and lower complementary inputs (generated from the input signal conditioner), $1/T_{u,lj}$ (*j*=1, 2) are the upper and lower BC drain currents and I_Q, I_o are biasing currents that control the quality factor *Q* and pole frequency ω_o, respectively. Finally, the positive factor *g* appearing in (3), was set equal to the biasing current I_o.

The LP and BP transfer functions implemented by the log-domain biquad of Fig. 7 are given by (8) and (9), whereas (10)describes the 2-pole, 1-zero transfer function required for the final OZGF channel. The transfer function in (10) is obtained by adding the biasing current I_Z at points *B* of Fig. 7 . By inspection: $\omega_o = I_o/nCV_T$, $Q = I_o/I_Q$ and the zero position is controlled by the ratio I_o/I_Z.

$$\frac{I_{OUT_{LP}}}{I_{IN}} = \frac{w_{u2} - w_{l2}}{{I_{IN}}^u - {I_{IN}}^l} = \frac{\left(I_o/nCV_T\right)^2}{s^2 + \frac{\left(I_o/nCV_T\right)}{\left(I_o/I_Q\right)}s + \left(I_o/nCV_T\right)^2} \tag{8}$$

$$\frac{I_{OUT_{BP}}}{I_{IN}} = \frac{w_{u1} - w_{l1}}{{I_{IN}}^u - {I_{IN}}^l} = \frac{\left(I_o/nCV_T\right)s}{s^2 + \frac{\left(I_o/nCV_T\right)}{\left(I_o/I_Q\right)}s + \left(I_o/nCV_T\right)^2} \tag{9}$$

$$\frac{I_{OUT_{2P1Z}}}{I_{IN}} = \frac{w_{u1} - w_{l1}}{{I_{IN}}^u - {I_{IN}}^l} = \frac{\left(\frac{I_o}{nCV_T}\right)\left[s + \frac{\left(I_o/nCV_T\right)}{\left(I_o/I_Z\right)}\right]}{s^2 + \frac{\left(I_o/nCV_T\right)}{\left(I_o/I_Q\right)}s + \left(I_o/nCV_T\right)^2} \tag{10}$$

B. The Input Signal Conditioner

For the input signal conditioner, we chose to implement the geometric mean splitter (GMS) for three reasons: a) it exhibits a good frequency response since it consists only from well-defined low-impedance points, b) it can be realized with few non-critical components and c) for its low DC levels, ensuring lower static power consumption and noise, relative to splitters employing the harmonic mean law.

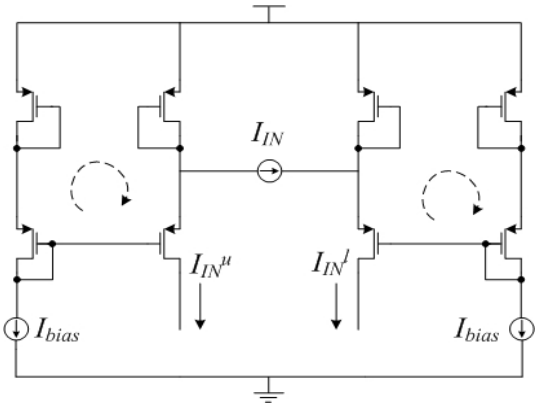

Fig. 6: PMOS-WI implementation of the geometric mean splitter.

Fig. 6 depicts the PMOS-WI GMS implementation used in this work. From the two (left and right) translinear loops, one may deduce that:

$${I_{IN}}^u \times {I_{IN}}^l = {I_{bias}}^2 (= {I_o}^2) \tag{11}$$

Also, it holds that:

$$I_{IN} = {I_{IN}}^u - {I_{IN}}^l \tag{12}$$

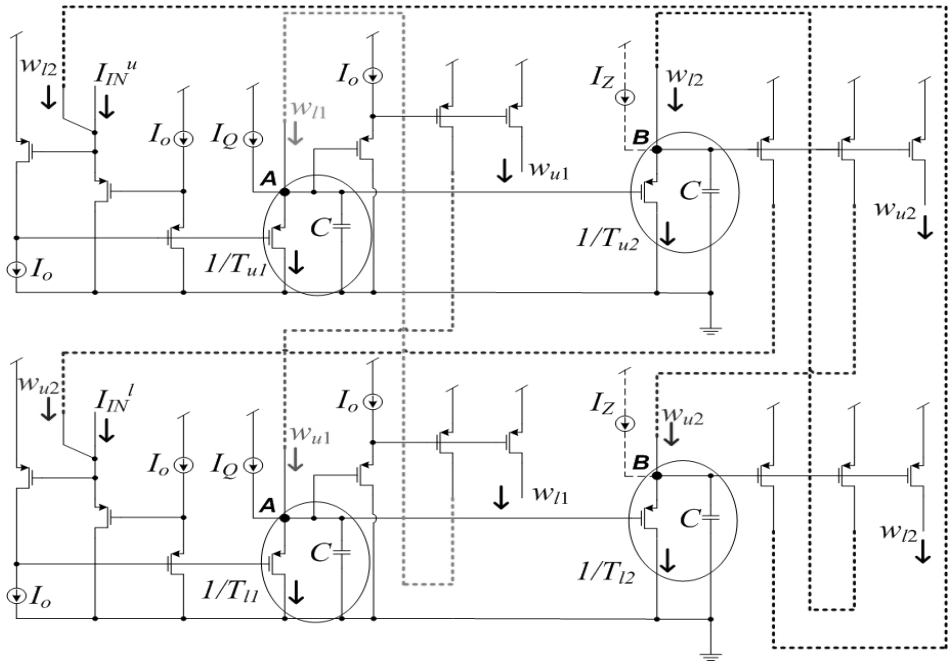

Fig. 7: The pseudo-differential Class-AB Log-domain Biquad. The design implements the state-space equations shown in (3). The feeding of the currents w_{u1} (w_{l1}) to the lower (upper) topology (implementing the linear and nonlinear cross-coupling terms to ensure correct Class-AB operation) is shown in dotted connections. All biasing current sources, as well as the subtraction of the *w* states to form the outputs, were facilitated by means of both PMOS and NMOS cascode current mirrors not shown for clarity.

Moreover, the large-signal expressions for the two positive, complementary, upper and lower, uni-directional currents are given by:

$$I_{IN}{}^{u} = \frac{I_{IN} + \sqrt{I_{IN}{}^{2} + 4I_o{}^{2}}}{2} \tag{13}$$

$$I_{IN}{}^{l} = \frac{-I_{IN} + \sqrt{I_{IN}{}^{2} + 4I_o{}^{2}}}{2} \tag{14}$$

Relations (11) and (12), together describe the splitting action and the law with which the two positive complementary inputs are defined. Fig. 8 illustrates typical current waveforms generated by the GMS used. The biasing current I_{bias} could in principle be set arbitrarily small to reduce the noise and static power, but in the subsequent OZGF implementation was set equal to I_o in order to ensure similar biasing conditions (and hence impedance levels) for all the transistors comprising the OZGF and reduce the overall number of external pin connections.

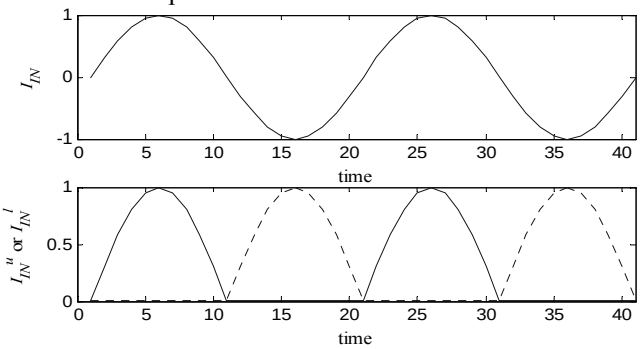

Fig. 8: Indicative current waveforms generated by the GMS. The upper (solid) and lower (dotted) complementary inputs resemble half-wave rectified signals.

Finally, it should be noted that one of the potential disadvantages of the GMS topology of Fig. 6, is the implementation of the floating current source I_{IN}. In practice, this current source was realized via two grounded AC current sources at an 180° phase difference with each other. The relative matching between the two sources will play a significant role in the linearity performance of the OZGF channel, since the performance of the whole system cannot exceed that of its input stage. This point will be addressed in more detail in a later section.

C. The Automatic Gain Control Circuits

The AGC should be designed in such a way so that a potentially wide DR at the input of the OZGF channel (greater than 5 orders of magnitude in this implementation) can be compressed to a small current range (typically within 1 order of magnitude) for the biasing current I_Q that sets the *Q*s of the biquads. Our AGC acts in feed-forward and consists of a cascade of four circuit blocks: a GMS, a low-frequency LP filter (LPF), an exponential transconductor (or E-cell) operating as a logarithmic transimpedance amplifier and a wide linear range OTA.

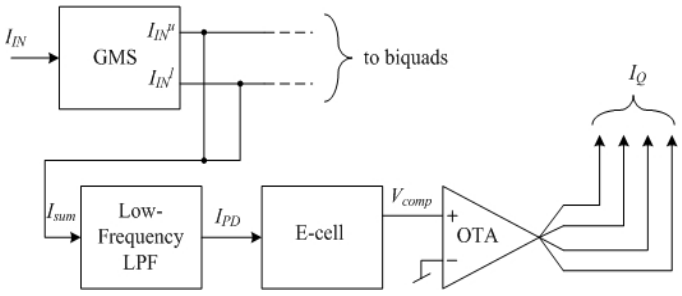

Fig. 9: Block diagram describing the processing stages of the AGC.

With the aid of Fig. 9, the processing stages can be summarized as follows:

- Stage 1: The GMS ensures that for small signals the OZGF gain does not exceed a certain value or shoot to instability (i.e. it sets the highest OZGF peak gain for zero input) and also full-wave rectifies the bi-directional input I_{IN} (I_{sum}).

- Stage 2: The low-frequency current-input current-output LPF gives a quasi-DC output (I_{PD}), whose value corresponds to the peak value of the full-wave rectified current input I_{sum}. In other words, the GMS together with the LPF implement a peak detector (i.e. full-wave rectification plus averaging).
- Stage 3: The E-cell compresses the, still wide, current range at the output of the LPF to a differential voltage range (V_{comp}) that can be easily accommodated by the OTA that follows. The compressive *I-V* transfer characteristic is electronically controlled by a single biasing current $I_{o\_control}$.
- Stage 4: The OTA converts V_{comp} to a DC current range, corresponding to the *Q* range of the OZGF. The tail current of the OTA (I_{tail}) together with $I_{o\_control}$ are the two main parameters that control the law with which the *Q* values are determined (i.e. which input strength value corresponds to which *Q*).

In the subsections that follow the AGC are described in detail.

AGC Stages 1 and 2: The GMS and Low-Frequency LPF

By adding the large-signal expressions of the two splitted complementary inputs (i.e. (13) and (14)) and by defining the peak values of the input as $\hat{I}_{IN} = m \times I_o$, with m[1] being the modulation index, we arrive at the following result:

$$\hat{I}_{sum} = \frac{\hat{I}_{IN} + \sqrt{\hat{I}_{IN}^{\,2} + 4I_o^{\,2}}}{2} + \frac{-\hat{I}_{IN} + \sqrt{\hat{I}_{IN}^{\,2} + 4I_o^{\,2}}}{2} = \sqrt{\hat{I}_{IN}^{\,2} + 4I_o^{\,2}} = I_o\sqrt{m^2+4} \quad (15)$$

The above relation states that for small m and less than 1 (i.e. when the biquads operate in their Class-A mode), $I_{sum}^{\max} \approx 2I_o$, whereas for $m \gg 1$, $\hat{I}_{sum} \approx mI_o = \hat{I}_{IN}$. In other words, for zero or small signals, the GMS outputs a current which has a minimum peak value close to $2I_o$, whereas for larger signals it follows the input peak almost exactly. Thus, by setting the control law to map the value $2I_o$ to the minimum I_Q value (corresponding to the maximum *Q*, since $Q=I_o/I_Q$), the OZGF channel will always have a bounded peak gain according to the required specifications and will never shoot-up to large unwanted gain values or instability. That is indeed a 'hidden' and very useful operation of the GMS, because it can rectify the input and set the highest bound for the OZGF peak gain in a simple and elegant manner without needing to resort to additional circuitry.

The current I_{sum} is consequently filtered by the low-frequency LPF to extract its DC component I_{PD}. However, to accurately obtain the peak value, I_{sum} needs to be multiplied by an appropriate scale factor. This multiplication factor, which is waveform dependent and was set here to $\pi/2$, was implemented by means of scaled current mirrors in the GMS. Since I_{sum} is a rectified positive current, the LPF does not have to operate in Class-AB mode. The LPF topology used in this work and depicted on Fig. 10, is a simple Class-A, 1st-order, log-domain integrator which implements the transfer function in (16). All symbols have their usual meaning.

$$H_{LPF}(s) = \frac{\omega_o'}{s+\omega_o'} = \frac{\left(I_{LPF}/nC_{LPF}V_T\right)}{s+\left(I_{LPF}/nC_{LPF}V_T\right)} \quad (16)$$

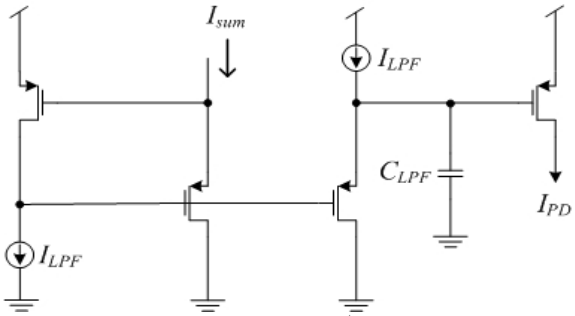

Fig. 10: The low-frequency LPF topology – A 1st-order Class-A log-domain integrator.

AGC Stage 3 and 4: The E-cell and wide linear range OTA

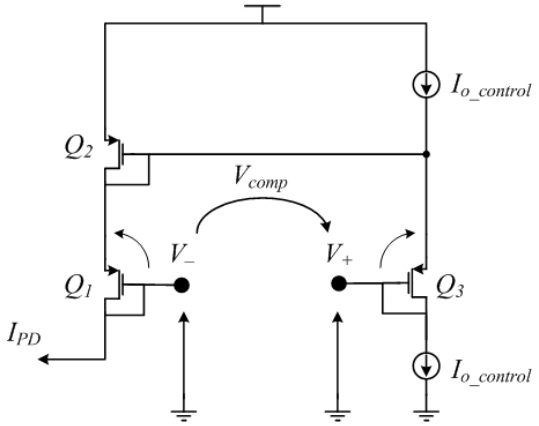

Fig. 11: The exponential transconductor – E-cell used for AGC action.

The E-cell, shown in Fig. 11, is an exponential transconductor operating as a nonlinear transimpedance amplifier. It consists of two low-impedance points (the drain-gates of devices Q_1 and Q_3) where the compressed differential voltage V_{comp} is generated when the current I_{PD} is sourced from the diode-connected drain of device Q_1. Device Q_2 serves as a degeneration (tail) resistor which, if appropriately sized, gives additional headroom for accommodating the upper biasing current source $I_{o\_control}$ (implemented by means of cascoded mirrors not shown for simplicity). The reason for using an E-cell compared to a standard diode to perform the logarithmic compression is attributed to the fact that with an E-cell the compressive *I-V* transfer characteristic can be electronically tuned by $I_{o\_control}$ as described by (17). From the translinear loop Q_1Q_3 and by assuming that $I_{Do1}=I_{Do3}$ (i.e. matched devices):

$$V_+ - nV_T \ln\left(\frac{I_{PD}}{I_{Do1}}\right) + nV_T \ln\left(\frac{I_{o\_control}}{I_{Do3}}\right) - V_- = 0 \Rightarrow V_+ - V_- = V_{comp} = nV_T \ln\left(\frac{I_{PD}}{I_{o\_control}}\right) \quad (17)$$

[1] The modulation index *m,* indicates how many times larger or smaller is the input zero-to-peak amplitude relative to the biasing current I_o.

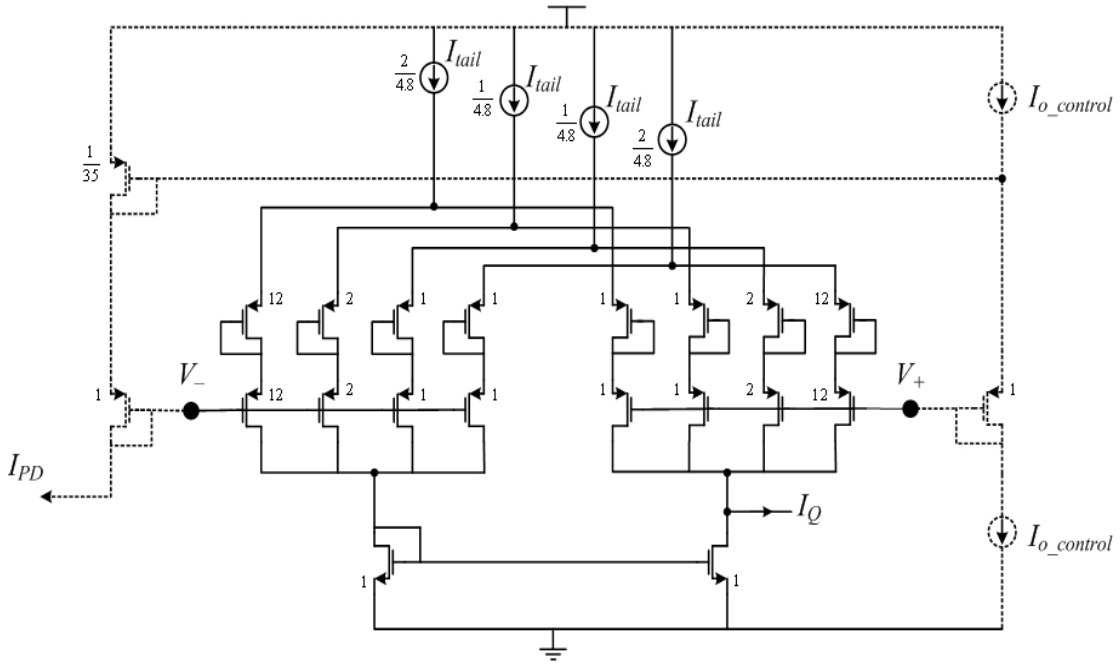

Fig. 12: The E-cell (dotted lines) connected together with a wide linear range OTA employing asymmetric cross-coupled, source-coupled pairs. The devices aspect ratios are indicated on the schematic.

The compressed differential voltage V_{comp} is subsequently applied to an OTA whose linear range was widened by using two standard techniques: a) plurality of cross-coupled, source-coupled pairs [42;43], and b) source degeneration. More specifically, four OTAs, each with an appropriate offset voltage and tail current, were degenerated and connected in tandem in order to realize an overall flatter input-output slope. This was achieved by choosing the offset voltages and tail currents in such a way so that the higher-order even and odd derivatives of the total (combined) transconductance become zero.

The offset voltages were realized by scaling asymmetrically the dimensions of the devices that comprise the branches of each OTA pair (see Fig. 12). In [43], for maximally flat transconductance characteristics, these aspect ratios were calculated to be 13.4, 2.04, 1, 1 and with tail current multiplication factors of 1.83, 1, 1, 1.83. However, since accurate linearity is not a crucial performance requirement for the AGC, the device aspect ratios and tail current multiplication factors were set to 12, 2, 1, 1 and 2, 1, 1, 2, respectively, in order to simplify our layout matching efforts during fabrication phase. The scaling factor of 4.8, which all the tail currents are divided with, was chosen empirically so that the upper and lower saturating levels of the *V-I* tanh function coincide with the actual I_{tail} value.

D. AGC Simulation Results

The simulation results presented in this section were obtained from Cadence IC Design Framework® and with the parameters presented in TABLE I. Indicative waveforms at the outputs of each AGC stage are shown, as well as the control law with which the I_Q values are determined. Fig. 13 shows the simulated *V-I* and transconductance transfer characteristics of the wide linear range OTA for an I_{tail} of 24nA. Strictly speaking the achieved linear input range is around $200\text{mV}_{\text{peak}}$. However, since the OTA operates in quasi-DC, the practically usable range is around $400\text{mV}_{\text{peak}}$. It should be noted that since $I_Q^{\max} \equiv I_{tail}$, the OTA sets the lowest bound of the OZGF peak gain according to $Q_{\min} = I_o / I_{tail}$. The control law was calibrated (via the currents $I_{o\_control}$ and I_{tail}) to map the minimum signal at the input of the OZGF (which results in a value of $2I_o \times (\pi/2)$ at the output of the LPF of the AGC) to a maximum biquad Q of 10. This corresponds to a value of 2nA for the respective I_Q currents and a nominal OZGF peak gain of ~80dB. On the other hand, for a maximum allowable input of 10μA (i.e. for m=500), the AGC gives an I_Q equal to 20nA corresponding to a Q of 1. Since I_{tail} sets the upper level of the *V-I* transfer characteristic of the OTA, for very large input signals (m > 500) the maximum I_Q value saturates at 24nA corresponding to a lowest Q of 0.834 and a passive OZGF peak gain of 1.43dB.

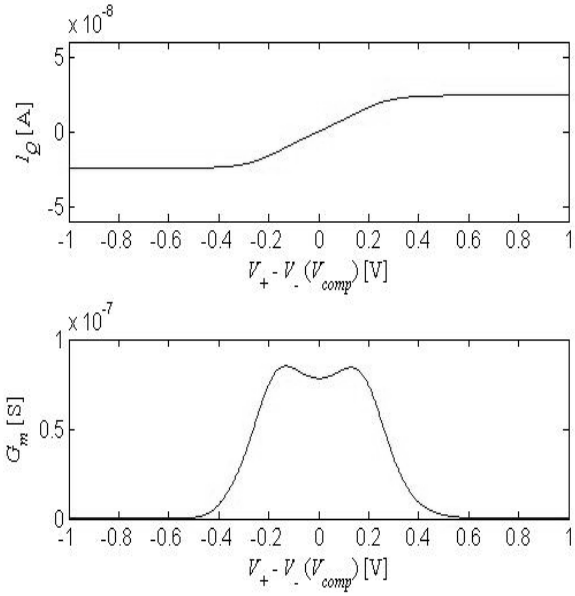

Fig. 13: *V-I* (upper) and transconductance (lower) simulated transfer characteristics of the wide linear range OTA for I_{tail} = 24nA.

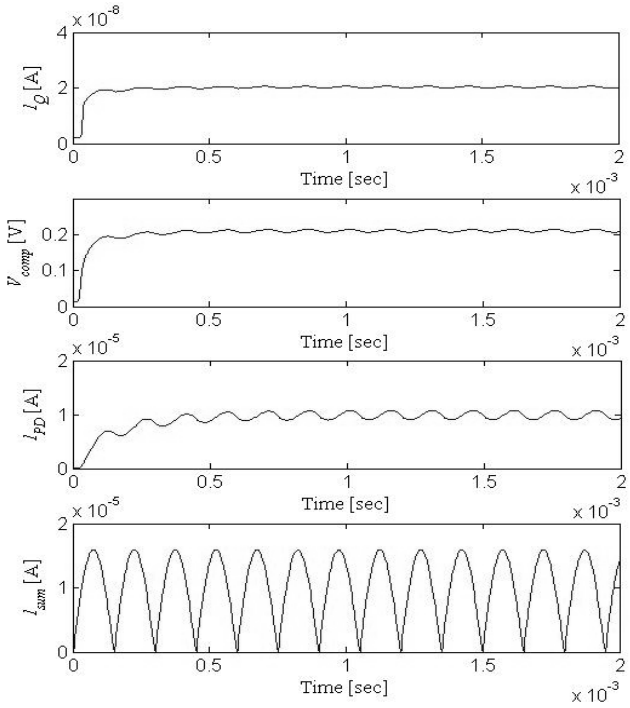

Fig. 14: Current waveforms from the output of each AGC stage for an input signal of m=500. Observe that the peak of I_{sum} is at ~16μA instead of 10μA (due to scaling by $\pi/2$), whereas the LP filtered version of I_{sum}, I_{PD}, is at 10μA as expected. The I_Q value is at 20nA corresponding to a Q of 1.

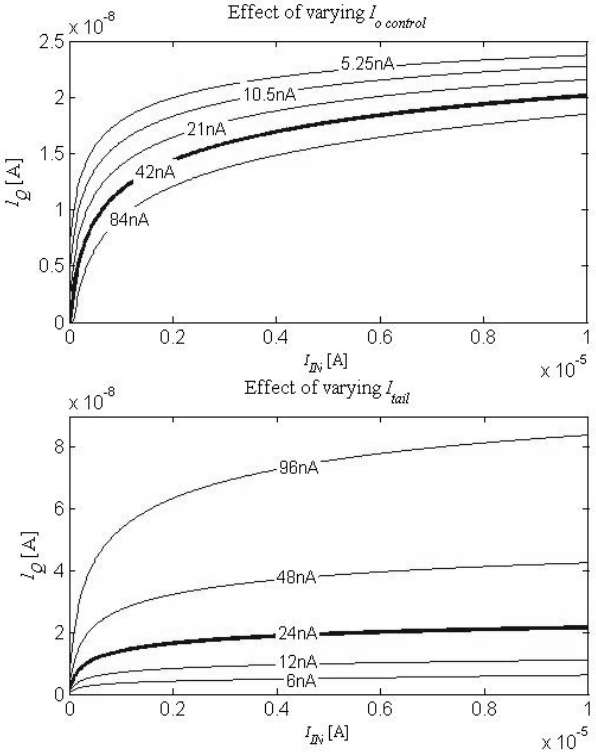

Fig. 15: Parametric DC response plots of the Q-control law with varying $I_{o\_control}$ (upper) or I_{tail} (lower). The bold curves are the ones corresponding to the values shown in TABLE I.

The law with which the Q values are determined was measured by performing a DC-sweep analysis on the whole AGC system. Fig. 15 depicts I_Q versus I_{IN} curves with $I_{o\_control}$ and I_{tail} as the two implicit parameters. It can be observed that the overall input-output AGC transfer characteristic is logarithmically compressive in nature as suggested by (17) with $I_{o\_control}$ controlling the 'vertical shift' of the characteristic and with I_{tail} controlling the actual level of compression as expected from (17) and OTA operation. Also observe that a linear change in I_{tail} results in a logarithmic change on the compression level, whereas a linear change in $I_{o\_control}$ results in a linear vertical shift of the whole characteristic. In conclusion, the above two electronically controllable degrees of freedom give a certain level of versatility to the AGC system because a variety of input DR values can be accommodated and mapped to a specific Q-range according to the particular physiological (modelling) or design (performance) specifications.

TABLE I
ELECTRICAL AND DEVICE PARAMETERS

Topology	Biquads	GMS	LPF	E-cell*	OTA*
$(W/L)_{PMOS}$	300μm/1.5μm				20μm/1.5μm
$(W/L)_{NMOS}$	60μm/8μm				10μm/1.5μm
I_o	20nA				
I_Q	2nA–24nA (i.e. Q between 0.834–10)				
I_Z	2nA (i.e. $0.1I_o$ for a –20dB DC gain)				
I_{LPF}	20nA				
$I_{o\_control}$	42nA				
I_{tail}	24nA				
V_{DD}	1.8V				
C	20pF				
C_{LPF}	80pF				

* The reported dimensions correspond to the minimum device sizes of Fig. 12.

VI. ACTIVE OZGF CHANNEL MEASURED RESULTS

The whole channel, together with its AGC, was integrated in the standard 0.35μm AMS 2P/4M CMOS process. The OZGF was tuned so that its nominal centre frequency (CF) falls at 3.3kHz for a Q of 1. This corresponds to I_o=I_Q=20nA.

Measurement Setup: In section V.B, it was mentioned that one of the disadvantages of the particular GMS topology was the need to accurately realize the floating current source I_{IN} in order to minimize distortion. In our case, this was achieved by using two 6221 precision AC/DC Keithley current sources. These were programmed using MatLab™ (via their GPIB interface) and triggered externally (using a TTL-compatible pulse from a Tektronix digital waveform generator) to output two AC current waveforms at an exact 180° phase difference with each other. Moreover, by fine-tuning their relative amplitudes and phases, we could partly overcome any mismatches between the two Class-A paths and consequently further optimize the linearity performance of the OZGF channel. A more economical alternative for realizing on-PCB these current sources is shown in Fig. 16 and includes: a) an audio-frequency transformer for generating two balanced differential voltages from a single-ended one, b) two resistors connected to a virtual ground for an accurate V-to-I conversion and c) two transconductance amplifiers (utilizing 100fA-leakage current Opamps) for buffering the output current. The relative mismatch of these current sources could be minimized by using low-tolerance (0.01%) metal foil resistors and with the transconductance amplifier output transistors being precisely matched on-chip. The OZGF output current was measured via standard I-to-V converters and through the 1MΩ input resistance of a Stanford Research 1mHz–100kHz spectrum analyzer (SRT785).

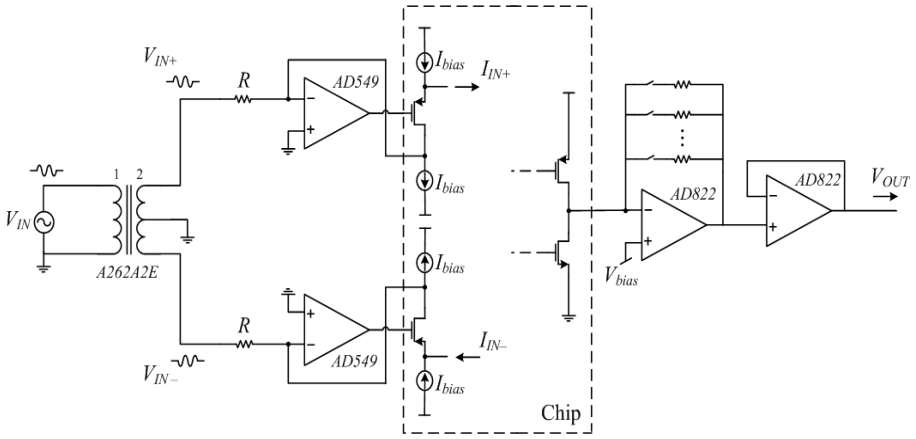

Fig. 16: Measuring setup for generating the two balanced bi-directional input currents (i.e. realizing the floating current I_{IN}). Since the transimpedance amplifiers operate in Class-A, the biasing currents I_{bias} should be set at a value equal to the maximum zero-to-peak amplitude of I_{IN}. The *I*-to-*V* conversion at the output of the last OZGF biquad is also shown.

Frequency Response: Fig. 17 shows the *Q*-tunability of the active 4th-order OZGF frequency response. The current I_Q was changed automatically via the action of the AGC by changing accordingly the strength of the input signal. Observe also that a linear change in I_Q corresponds to a logarithmic change in the peak gain (or *Q*) due to a) the compressive law of the AGC and b) due to the fact that $Q=I_o/I_Q$; this is indeed another form of compressive behavior which is embedded in the frequency response and stems directly from the design equations of the log-domain biquads. Fig. 19 shows tuning of the OZGF's low-frequency tail by varying the current I_Z, whereas Fig. 18 shows the three-orders of magnitude ω_o-tunability when changing the biasing current I_o to 2, 20 and 200nA, successively. For each ω_o, two indicative *Q* setups are shown to demonstrate gain adaptation within the whole audio spectrum. Observe the quite stable characteristics over frequency. Also note that the low-ω_o, high-*Q* response is affected by input signal noise because of the low biasing current levels of the particular configuration. Finally, it should be emphasized that all low-to-moderate *Q* responses were obtained with a large *m* (> 10) in order to validate the OZGF's Class-AB operation.

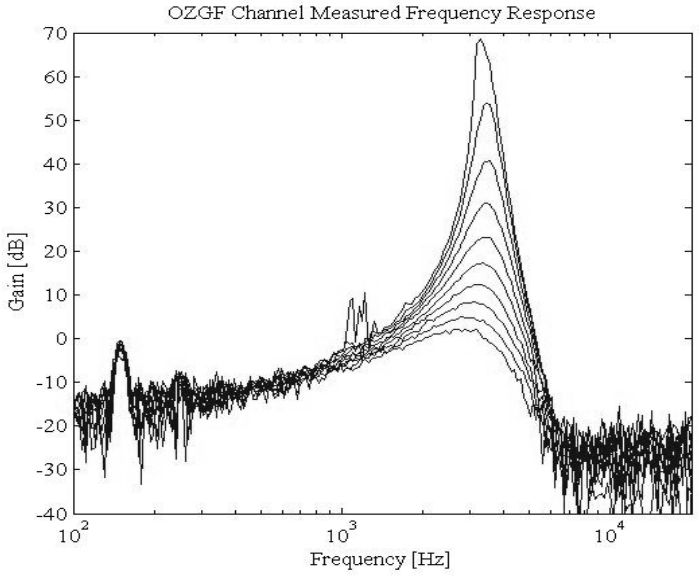

Fig. 17: *Q*-tunability of the active 4th-order OZGF frequency response. The maximum peak gain was measured at 70dB.

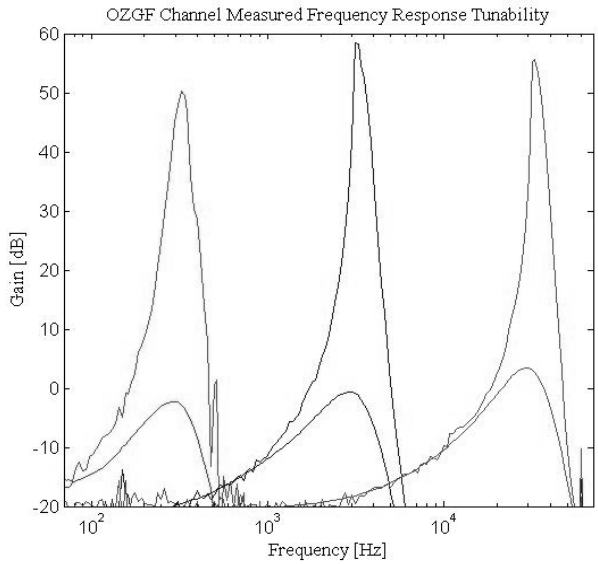

Fig. 18: Gain adaptation and ω_o-tunability (CF from 330Hz to 33kHz).

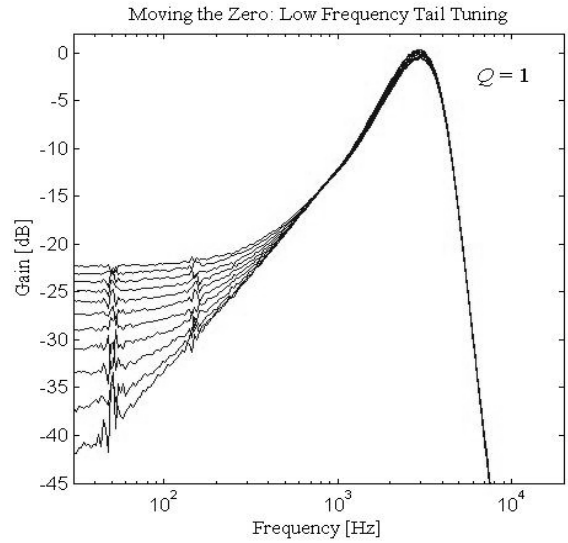

Fig. 19: Low-frequency tail tuning by means of varying the biasing current I_Z.

Total Harmonic Distortion (THD): The THD is a common measure for assessing the linearity performance of amplifier systems. However when talking about audio/auditory processors, its value must be appropriately judged since the 'shape' of a signal's

spectrum is something that affects one's hearing perception. In other words, a signal with a certain THD value might sound 'aesthetically more pleasing' to our ears than an other of equal or lower THD value. In commercial and academic cochlea designs a common upper limit for THD is 4-5% (e.g. Sarpeshkar's cochlea: <4%, MED-EL's state-of-the-art DUET EAS hearing system: <5%@500Hz, Phonak Super-Front PPC-4 <7%@500Hz etc.). This was also justified experimentally from a recent (and one of the first) log-domain implementations of a CMOS cochlea, where the effect of distortion started to become evident to the ear after 5% THD [44]. Finally, note that the 10%@1kHz THD value represents a desirable amount of allowable distortion for typical low-cost wide-band audio material such as FM broadcasts, CD-media or cassette tape media. For these reasons, we decided to set the upper limit of THD to about 5% for our OZGF cochlea channel.

Due to their differential nature, CMOS-WI Class-AB log-domain filters exhibit mainly odd-harmonic distortion content. Their THD (for frequencies near the pole frequency) usually reaches the 1% value quite early (for m values as low as 1, i.e. at the border between Class-A and Class-AB operation), but grows rather slowly thereafter; this behavior renders log-domain filters as adequate candidates for applications where moderate THD values can be tolerated. Fig. 22 shows THD versus input strength (m) for various tones near-and-at the CF and deep in the passband for the open-loop Q=1 OZGF response. At the CF, the THD for an input of 10μA (m = 500) is at 3.5%. Fig. 23 shows how the active OZGF adapts automatically its peak gain with input level together with the corresponding output THD. For a 14pA input tone the OZGF provides a peak gain of 70dB at 0.4% output THD, whereas for an input tone of 10μA, the peak gain is at –0.98dB with an output THD of 3.5%.

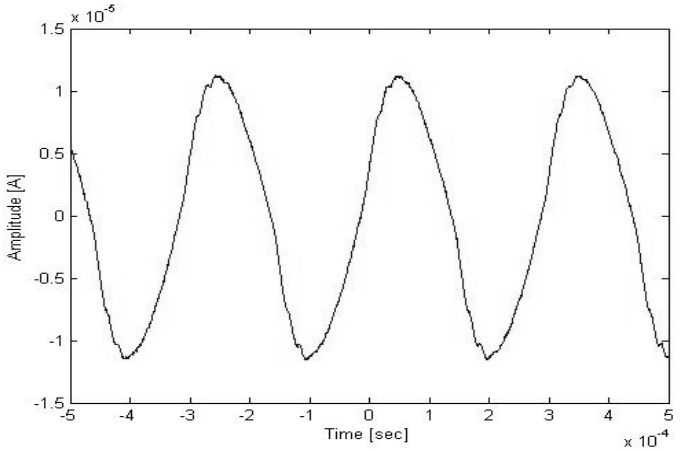

Fig. 20: Indicative distortion at the output for a sinusoidal input at a frequency near CF. For this particular waveform the THD is a bit above 4%.

Two-Tone Intermodulation Tests: Fig. 24 shows both even- and odd-order measured intermodulation distortion products (IMD) for two tones placed at a frequency ±2% away from the (CF) 3kHz of the open-loop Q=1 OZGF response. The IMD_2 starts at around –34dB for small-signals and increases gradually to higher dB values with f_2–f_1 increasing faster than f_1–f_2. The IMD_3 is less attractive with a much unpredictable behavior towards smaller signals. These results are illogical and unfortunately do not compare favorably to IMD figures reported from similar (biquadratic and not) CMOS-WI log-domain efforts [16;45] – even though those were only IMD_2 (a quite unreasonable test for differential filters), they were obtained at ±10% of a given frequency and for lower-order filters with some gain. We believe that our results can be improved considerably in future implementations, nonetheless one should appreciate that the real cochlea exhibits a considerable intermodulation distortion, with both its $IMD_{2,3}$ levels around –20dB for large inputs (see Fig. 21).

In any case, we have managed recently to identify some potential optimization steps that may lead to an improved overall intermodulation linearity performance. We are currently working on a 2nd-generation, 4th-order OZGF channel which, in simulation, exhibits IMD_3 levels below –35dB for small-signals and which also stay below –25dB across the whole input range (see Fig. 25).

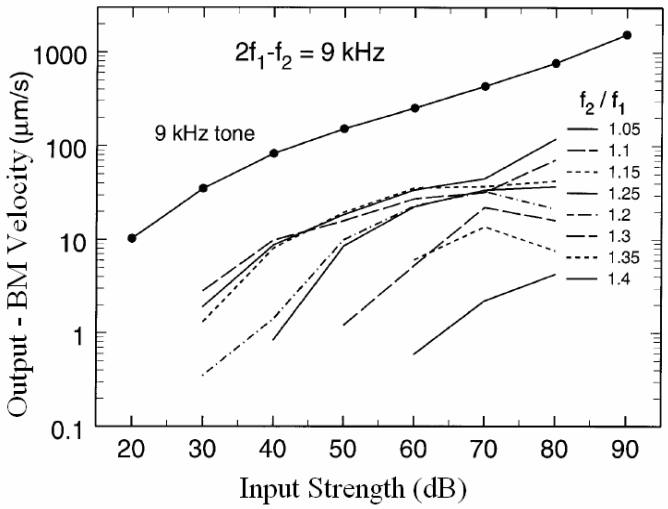

Fig. 21: Growth of the IMD_3 as a function of the signal strength of two equal-level tones in the real cochlea. The solid circle curve is the output from a single tone at the distortion product frequency i.e. CF = $2f_2$–f_1. All other curves are the magnitudes of the cubic distortion products as a function of input strength for several frequency ratios f_2/f_1. At f_2/f_1 = 1.05, corresponding to ±2%, the IMD_3 is around -17dB below the fundamental; adapted from Robles [46].

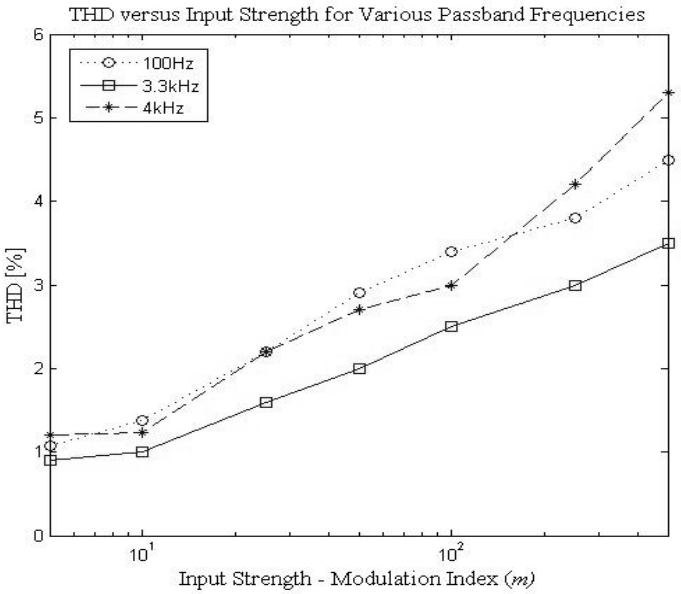

Fig. 22: Measured single-tone linearity of the 4th-order OZGF for various passband frequencies.

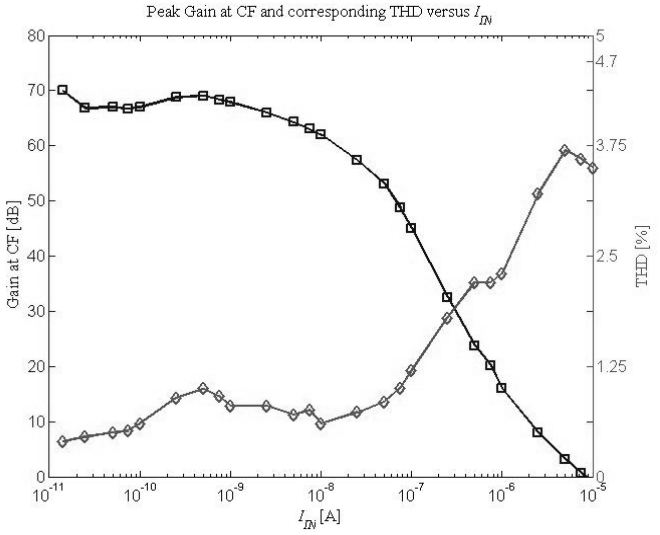

Fig. 23: Measured peak gain at CF and corresponding output THD vs. I_{IN}.

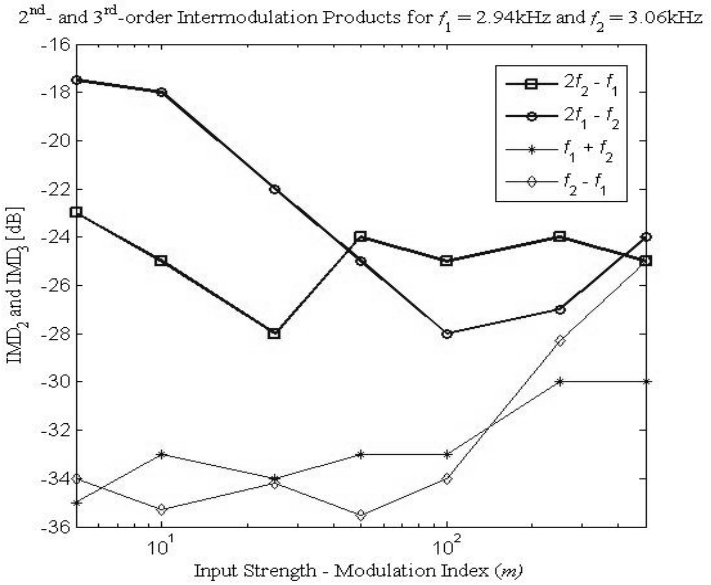

Fig. 24: Measured two-tone 3rd- and 2nd-order intermodulation products of the 4th-order OZGF for two frequencies at ±2% away from 3kHz.

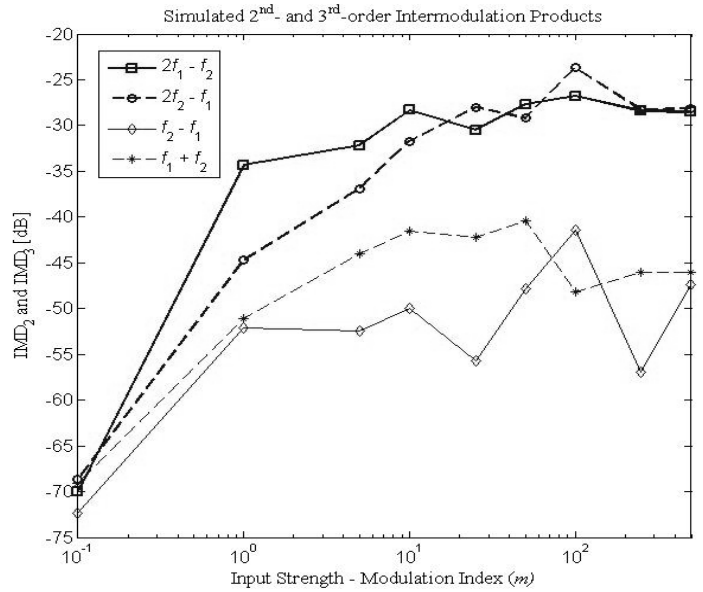

Fig. 25: Simulated two-tone 3rd- and 2nd-order intermodulation products of the 2nd-generation 4th-order OZGF for two frequencies at ±2% away from 3kHz.

Mismatch: One potential disadvantage of all pseudo-differential Class-AB filters of the type shown in Fig. 7 is that any potential mismatch between the two signal paths translates to distortion at the output. Therefore, considerable attention was given during layout in order to try and accurately match the two Class-A branches. Specifically, the two (upper and lower) translinear loops comprising each Class-A biquad, were nested together in such a way so that every upper transistor was interdigitized with its corresponding lower counterpart. Common centroid arrangements along both axes of symmetry were also employed. Fig. 26 shows Q=1 and Q=10 measured OZGF frequency responses across 19 chips. Observe that in both cases the relative variation between responses does not exceed 6dB.

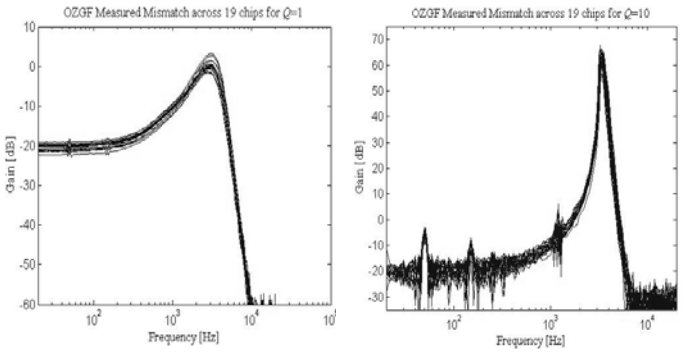

Fig. 26: OZGF mismatch across 19 chips for both extreme cases of Q.

Input Dynamic Range (DR): In this work, by input DR we imply the ratio of the maximum input signal for a given allowable distortion at the output (measured in % of THD) over the noise floor for zero input. The measured input DR was calculated by taking into consideration the compressive action of the AGC by dividing the maximum signal at the input of the passive (Q=1) OZGF response over the measured noise floor (integrated over the 3dB bandwidth) of the fully active (Q=10) OZGF response. The maximum input DR at CF was found to be 124dB at <5% THD, although at different frequencies this figure changed – since the distortion is not uniform across the whole bandwidth of the OZGF. More specifically, we observed an abrupt increase in THD around 1/3 of the CF; a problem partially attributed to the fact that at 1/3 of the CF the input tone experiences a gain of ~ –10dB, whereas the 3rd-harmonic (which is generated and propagated across the 4 log-domain biquads) a gain of ~2dB. In other words, the fundamental gets suppressed, whereas the distortion gets amplified. Moving deeper in the passband one would expect that this particular problem would become more severe since both the 3rd and 5th harmonics would get amplified while the fundamental would get suppressed even further. However this is not entirely the case, because for low frequencies the whole structure operates virtually at DC, the capacitors draw smaller currents and hence the exerted nonlinearities are weaker.

It is really interesting to notice that the aforementioned phenomenon (that of 'amplified distortion' as opposed to the more common 'distorted amplification') is also observed in the biological cochlea. Recent measurements in the basal turn of the guinea-pig cochlea [47] revealed that the real cochlea exhibits even-order harmonic content with maximum second-order harmonic distortion levels of 4% and 28% near and at half an octave below the CF respectively. These results are illustrated in Fig. 27 for convenience. Since our implementation contains odd-harmonic con-

tent, we expect the maximum distortion to occur at 1/3 of the CF, which indeed was the case.

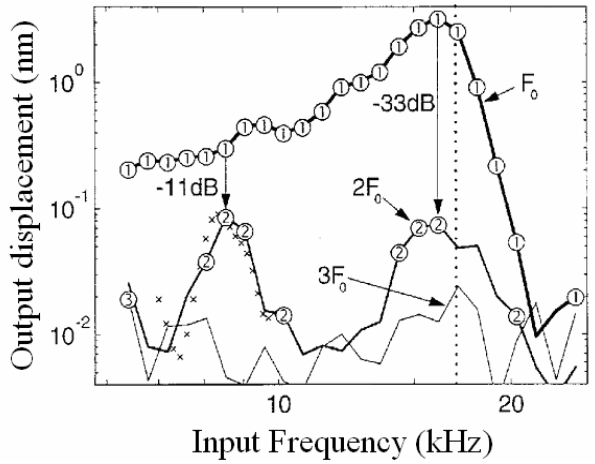

Fig. 27: Indicative harmonic distortion in the guinea-pig cochlea to a moderately loud sound burst (60dB). Note the two distinct frequency peaks of the second harmonic; adapted from Cooper [47].

Out-of-Band Interferer: A well-known problem of all ELIN topologies is that their noise floor is signal-dependent resulting in a constant output SNR of about 60dB for large m values. One manifestation of this problem is the ability of the filter to maintain good signal integrity at the presence of an out-of-bound interferer. Fig. 28 shows the measured PSD of an 1μA (m=10) in-band signal at CF. An out-of-band interferer was placed at 20kHz and for two distinct amplitudes, 1μA and 10μA. It was observed that the noise PSD increased from around –60dB for the case of an absent interferer to about –40dB for the case of the 10μA interferer; that is about 10dB per decade of interferer amplitude increase as predicted in [48] and experimentally verified in [45].

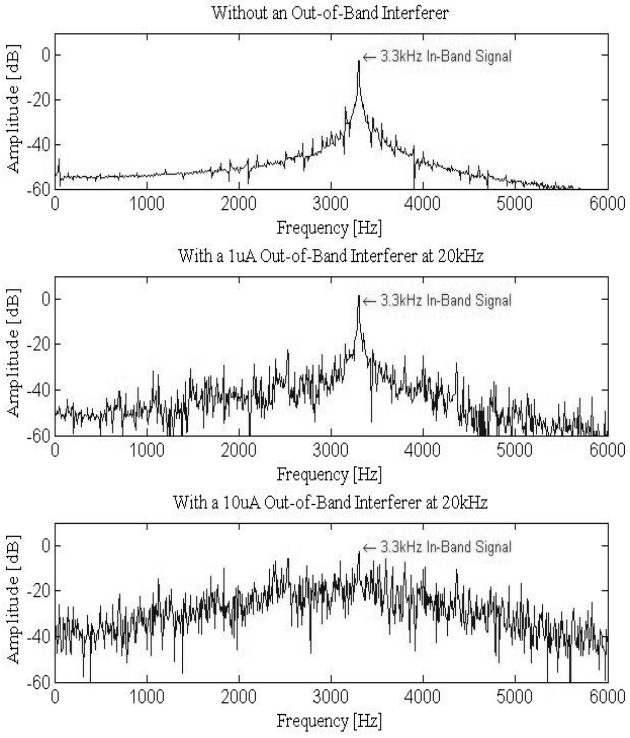

Fig. 28: Masking effect of an out-of-band interferer.

TABLE II summarizes the measured performance of the active 4th-order OZGF cochlea channel, whereas Fig. 29 shows a chip micrograph of the channel's layout.

TABLE II
OZGF MEASURED PERFORMANCE

Power Consumption	3.4μW (no AGC), 4.46μW (with AGC)
Noise Floor	67.5pA (Q=1), 14pA (Q=10)
Bandwidth (CF)	3.3kHz (Q=1)–3.7kHz (Q=10)
Peak Gain	70dB with <1% THD
Input DR at CF	124dB with <5% THD (with AGC)
SNR at CF	~60dB for m>10
Total on-chip capacitance	400pF
Chip area	1.5mm×1.5mm (2.25mm^2)

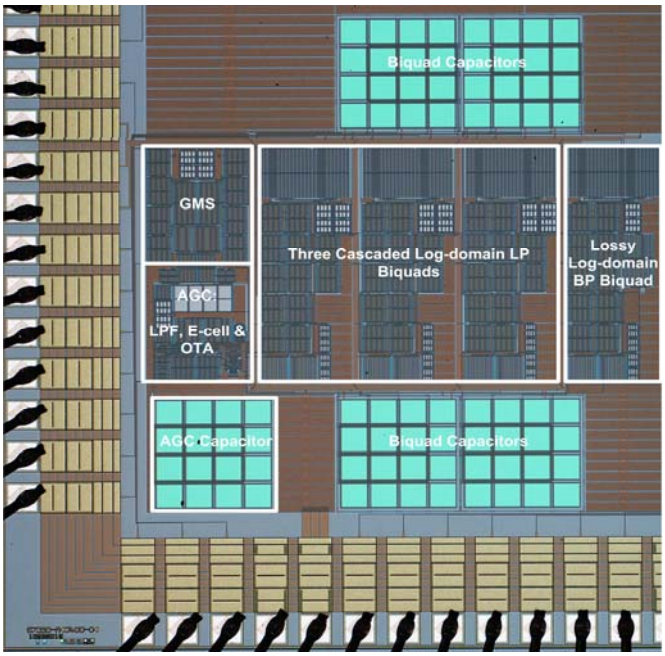

Fig. 29: Chip micrograph of the 4th-order OZGF channel with the AGC.

VII. SUMMARY, DISCUSSION & CONCLUSION

Our architectural choices and measured results can be summarized in the following points:

- Instead of opting for a filter-cascade implementation, which is prone to noise and offset accumulation, gain sensitivity and yield, our design is based on separate filterbank channels of short-cascades. In this way, we were able to model the propagation of distortion products, conserve on computation and obtain realistic roll-off slopes, amplitude and group-delay responses without the associate disadvantages of long-cascade models.
- The real cochlea exhibits 120dB of input dynamic range at 3kHz at <5% THD. Our measured results at the exact same frequency revealed an input DR of 124dB at <5% THD.
- The basilar membrane in the real cochlea has an area of approximately 70mm^2. This is equivalent to having a filterbank employing approximately thirty 4th-order OZGF channels.
- A linear change in Q results in a logarithmic change in the peak gain (and in the temporal resolution) of our log-domain OZGF response (see Fig. 17). Contrary to prior

cochlea implementations, this is compatible with biology (see Fig. 1 and its caption). It is interesting to note that from Fig. 1 and 17 one could qualitatively extrapolate on the actual *Q*-control law the real cochlea is performing.

- Our 4th-order OZGF frequency response achieves 70dB of amplification for small-signals (even though in practice we could get gains as high as 100dB), while maintaining a linear low-frequency tail (20dB/Dec) with steep high-frequency roll-off slopes (–160dB/Dec).
- Our AGC dissipates 1μW and compresses the 6 orders of magnitude of input signal intensity into 1 decade of *Q*-value tuning range. Moreover it sets the lower and upper bounds of the peak-gain response avoiding excessive distortion or instability. In addition, asymmetric attack and release time constant programmability can be easily incorporated by modifying the LPF like in [49]. Lastly, in this implementation the AGC acts in feed-forward and takes as input the global input. The downside of such a scheme is that the AGC does not contain any frequency information. The AGC can become frequency-dependent by modifying the architecture to accept as an input the output from the 1st LP OZGF stage or the output from the last BP OZGF stage (in that case the AGC regulation will be closed-loop).

All the circuits presented in this work may serve as basic building blocks for the realization of new biorealistic cochlea processors designed in any of the two commonly-used architectures; filterbank or filter-cascade. Nonetheless, we believe that the 4th-order OZGF channel presented here is a good compromise between biorealism, circuit complexity and yield and may be suitable in filterbank applications were biological fidelity and/or high DR performance is of primary interest. The choice for using CMOS-WI pseudo-differential Class-AB log-domain biquads for low-power, high DR operation has proven successful at the expense of an increased chip area, since the capacitor and transistor count increases by a factor of 2. Future generations of OZGF channels are part of our on-going research efforts in an attempt to increase the overall performance while reducing the per channel area. On this note, we have recently managed to design a current-mode integrator that achieves companding via the hyperbolic sine (*sinh*) law instead of the logarithmic. The result is a simple circuit that operates inherently in Class-AB, requires only one capacitor to realize a single pole, dissipates a mere 0.35μW of power and achieves 120+dB of input DR at <4% THD without an AGC [50]. A thorough evaluation with insights on the integrator's operation and optimization will appear shortly in [51].

ACKNOWLEDGEMENT

The authors will like to thank the Engineering and Physical Science Research Council (EPSRC) UK for funding this work.

REFERENCES

[1] C. Mead, "Neuromorphic electronic systems," *Proceedings of the IEEE*, vol. 78, no. 10, pp. 1629-1636, 1990.

[2] R. Lyon, "A computational model of filtering, detection, and compression in the cochlea," in *Acoustics, Speech, and Signal Processing, IEEE International Conference on ICASSP '82,* 7 ed 1982, pp. 1282-1285.

[3] R. F. Lyon and C. Mead, "An analog electronic cochlea," *Acoustics, Speech, and Signal Processing, IEEE Transactions on*, vol. 36, no. 7, pp. 1119-1134, 1988.

[4] R. F. Lyon and C. A. Mead, "A CMOS VLSI cochlea," *Acoustics, Speech, and Signal Processing, 1988. ICASSP-88. , 1988 International Conference on*, pp. 2172-2175, 1988.

[5] Lyon R.F. and C. Mead, "Electronic Cochlea," in *Analog VLSI and Neural Systems* Addison-Wesley: 1989, pp. 279-302.

[6] R. F. Lyon, "Analog Implementations of Auditory Models," *DARPA Workshop on Speech Recognition and Natural Language*, 1991.

[7] L. Watts, D. A. Kerns, R. F. Lyon, and C. A. Mead, "Improved implementation of the silicon cochlea," *Solid-State Circuits, IEEE Journal of*, vol. 27, no. 5, pp. 692-700, 1992.

[8] A.Van Schaik, E.Fragniere, and E.Vittoz, "Improved Silicon Cochlea using Compatible Lateral Bipolar Transistors," in *Advances in Neural Information Processing Systems 8*. D.Touretzky et al., Ed. Cambridge MA: MIT press, 1996, pp. 671-677.

[9] R. Sarpeshkar, R. F. Lyon, and C. A. Mead, "An analog VLSI cochlea with new transconductance amplifiers and nonlinear gain control," *Circuits and Systems, 1996. ISCAS '96. , 'Connecting the World'. , 1996 IEEE International Symposium on*, vol. 3, pp. 292-296, 1996.

[10] R. Sarpeshkar, Lyon R.F., and C. Mead, "A Low-Power Wide-Dynamic-Range Analog VLSI Cochlea," *Analog Integrated Circuits and Signal Processing*, vol. 13, pp. 123-151, 1997.

[11] R. Sarpeshkar, "Efficient Precise Computation with Noisy Components: Extrapolating From an Electronic Cochlea to the Brain." PhD Thesis, California Institute of Technology, 1997.

[12] N. A. Bhadkamkar, "Binaural source localizer chip using subthreshold analog CMOS," in *Neural Networks, 1994. IEEE World Congress on Computational Intelligence., 1994 IEEE International Conference on,* 3 ed 1994, pp. 1866-1870.

[13] Cornil J.P. and Jespers P.G.A., "A micropower switched capacitor implementation of the silicon cochlea," 1994, pp. 100-103.

[14] P. M. Furth and A. G. Andreou, "A design framework for low power analog filter banks," *Circuits and Systems I: Fundamental Theory and Applications, IEEE Transactions on*, vol. 42, no. 11, pp. 966-971, 1995.

[15] J. Georgiou and C. Toumazou, "A 126-/spl mu/W cochlear chip for a totally implantable system," *Solid-State Circuits, IEEE Journal of*, vol. 40, no. 2, pp. 430-443, 2005.

[16] I. Grech, J. Micallef, and T. Vladimirova, "Low-Power Log-Domain CMOS Filter Bank for 2-D Sound Source Localization," *Analog Integrated Circuits Signal Processing*, vol. 36, no. 1-2, pp. 99-117, 2003.

[17] Lazzaro J., "Silicon models of early audition." PhD Thesis, California Institute of Technology, 1990.

[18] W. Liu, A. G. Andreou, and M. H. Goldstein, "Voiced-speech representation by an analog silicon model of the auditory periphery," *Neural Networks, IEEE Transactions on*, vol. 3, no. 3, pp. 477-487, 1992.

[19] B. Wen and K. Boahen, "A 360-Channel Speech Preprocessor that Emulates the Cochlear Amplifier," *Solid-State Circuits, 2006 IEEE International Conference Digest of Technical Papers*, pp. 2268-2277, 2006.

[20] C. Vincent, L. Shih-Chii, and V. S. Andre, "AER EAR: A Matched Silicon Cochlea Pair With Address Event Representation Interface," *Circuits and Systems I: Regular Papers, IEEE Transactions on*, vol. 54, no. 1, pp. 48-59, 2007.

[21] R. Sarpeshkar, C. Salthouse, S. Ji-Jon, M. W. Baker, S. M. Zhak, T. K. T. Lu, L. Turicchia, and S. Balster, "An ultra-low-power programmable analog bionic ear processor," *Biomedical*

Engineering, IEEE Transactions on, vol. 52, no. 4, pp. 711-727, 2005.

[22] P. I. M. Johannesma, "The pre-response stimulus ensemble of neuron in the cochlear nucleus," *Proceedings of the Symposium of Hearing Theory*, 1972.

[23] R. F. Lyon, "The all-pole gammatone filter and auditory models," *Acustica*, vol. 82, p. S90, 1996.

[24] R. D. Patterson and I. Nimmo-Smith, "Off-frequency listening and auditory-filter asymmetry," *The Journal of the Acoustical Society of America*, vol. 67, no. 1, pp. 229-245, Jan.1980.

[25] T. Irino, "An optimal auditory filter," *Applications of Signal Processing to Audio and Acoustics, 1995. , IEEE ASSP Workshop on*, pp. 198-201, 1995.

[26] T. Irino and R. D. Patterson, "A compressive gammachirp auditory filter for both physiological and psychophysical data," *The Journal of the Acoustical Society of America*, vol. 109, no. 5, pp. 2008-2022, May2001.

[27] T. Irino and R. D. Patterson, "A time-domain, level-dependent auditory filter: The gammachirp," *The Journal of the Acoustical Society of America*, vol. 101, no. 1, pp. 412-419, Jan.1997.

[28] Slaney M., "An Efficient Implementation of the Patterson-Holdsworth Auditory Filter Bank,"Apple Technical Report #35, 1993.

[29] Katsiamis A.G., E. M. Drakakis, and R. F. Lyon, "Practical Gammatone-like Filters for Auditory Processing," *EURASIP Journal on Audio, Speech, and Music Processing*, vol. 2007, 15 Pages, 2007.

[30] M. A. Ruggero, S. S. Narayan, A. N. Temchin, and A. Recio, "Mechanical bases of frequency tuning and neural excitation at the base of the cochlea: Comparison of basilar-membrane vibrations and auditory-nerve-fiber responses in chinchilla," *PNAS*, vol. 97, no. 22, pp. 11744-11750, Oct.2000.

[31] Y. Tsividis, "Externally linear, time-invariant systems and their application to companding signal processors," *Circuits and Systems II: Analog and Digital Signal Processing, IEEE Transactions on*, vol. 44, no. 2, pp. 65-85, 1997.

[32] D. R. Frey, "Exponential state space filters: a generic current mode-design strategy," *Circuits and Systems I: Fundamental Theory and Applications, IEEE Transactions on*, vol. 43, no. 1, pp. 34-42, 1996.

[33] Y. Tsividis, "On linear integrators and differentiators using instantaneous companding," *Circuits and Systems II: Analog and Digital Signal Processing, IEEE Transactions on*, vol. 42, no. 8, pp. 561-564, 1995.

[34] D. R. Frey, "Log-domain filtering: an approach to current-mode filtering," *Circuits, Devices and Systems, IEE Proceedings G*, vol. 140, no. 6, pp. 406-416, 1993.

[35] R. M. Fox, "Enhancing dynamic range in differential log-domain filters based on the two-filters approach," *Circuits and Systems, 2000. Proceedings. ISCAS 2000 Geneva. The 2000 IEEE International Symposium on*, vol. 2, pp. 617-620, 2000.

[36] D. R. Frey and A. T. Tola, "A state-space formulation for externally linear class AB dynamical circuits," *Circuits and Systems II: Analog and Digital Signal Processing, IEEE Transactions on*, vol. 46, no. 3, pp. 306-314, 1999.

[37] D. R. Frey and Y. P. Tsividis, "Syllabically companding log domain filter using dynamic biasing," *Electronics Letters*, vol. 33, no. 18, pp. 1506-1507, 1997.

[38] Y. Tsividis, "Minimising power dissipation in analogue signal processors through syllabic companding," *Electronics Letters*, vol. 35, no. 21, pp. 1805-1807, 1999.

[39] E. Fragniere, A. van Schaik, and E. A. Vittoz, "Design of an Analogue VLSI Model of an Active Cochlea," *Analog Integrated Circuits and Signal Processing*, vol. 13, no. 1, pp. 19-35, May1997.

[40] E. M. Drakakis, A. J. Payne, and C. Toumazou, "Log-domain filtering and the Bernoulli cell," *Circuits and Systems I: Fundamental Theory and Applications, IEEE Transactions on*, vol. 46, no. 5, pp. 559-571, 1999.

[41] E. M. Drakakis, A. J. Payne, and C. Toumazou, "'Log-domain state-space': a systematic transistor-level approach for log-domain filtering," *Circuits and Systems II: Analog and Digital Signal Processing, IEEE Transactions on*, vol. 46, no. 3, pp. 290-305, 1999.

[42] K. Kimura, "The ultra-multi-tanh technique for bipolar linear transconductance amplifiers," *Circuits and Systems I: Fundamental Theory and Applications, IEEE Transactions on*, vol. 44, no. 4, pp. 288-302, 1997.

[43] H. Tanimoto, M. Koyama, and Y. Yoshida, "Realization of a 1-V active filter using a linearization technique employing plurality of emitter-coupled pairs," *Solid-State Circuits, IEEE Journal of*, vol. 26, no. 7, pp. 937-945, 1991.

[44] "Personal Communication with Dr Julius Georgiou," 2007.

[45] D. Python and C. C. Enz, "A micropower class-AB CMOS log-domain filter for DECT applications," *Solid-State Circuits, IEEE Journal of*, vol. 36, no. 7, pp. 1067-1075, 2001.

[46] L. Robles, M. A. Ruggero, and N. C. Rich, "Two-Tone Distortion on the Basilar Membrane of the Chinchilla Cochlea," *J Neurophysiol*, vol. 77, no. 5, pp. 2385-2399, 1997.

[47] N. P. Cooper, "Harmonic distortion on the basilar membrane in the basal turn of the guinea-pig cochlea," *The Journal of Physiology*, vol. 509, no. 1, pp. 277-288, 1998.

[48] C. Enz, M. Punzenberger, and D. Python, "Low-voltage log-domain signal processing in CMOS and BiCMOS," *Circuits and Systems II: Analog and Digital Signal Processing, IEEE Transactions on*, vol. 46, no. 3, pp. 279-289, 1999.

[49] S. M. Zhak, S. M. Zhak, M. W. Baker, and R. Sarpeshkar, "A low-power wide dynamic range envelope detector A low-power wide dynamic range envelope detector," *Solid-State Circuits, IEEE Journal of*, vol. 38, no. 10, pp. 1750-1753, 2003.

[50] A. G. Katsiamis, Ip H.M.D, and E. M. Drakakis, "A Practical CMOS Companding Sinh Lossy Integrator," *In Proceedings of the International Symposium on Circuits and Systems, 27-30 May 2007, New Orleans*, 2007.

[51] A. G. Katsiamis, Glaros K.N., and E. M. Drakakis, "Insights and Advances on CMOS Sinh Companding Filters," *To appear in Circuits and Systems I: Fundamental Theory and Applications, IEEE Transactions on*, 2008.